

# A scanning transmission X-ray microscope at the Pohang Light Source

Hyun-Joon Shin,\* Namdong Kim, Hee-Seob Kim, Wol-Woo Lee,  
Chae-Soon Lee and Bongsoo Kim

Pohang Accelerator Laboratory, POSTECH, 127 Jigok-ro, Nam-gu, Pohang-si, Gyeongsangbuk-do 37673, Republic of Korea. \*Correspondence e-mail: shj001@postech.ac.kr

Received 8 January 2018

Accepted 12 February 2018

Edited by R. W. Strange, University of Essex, UK

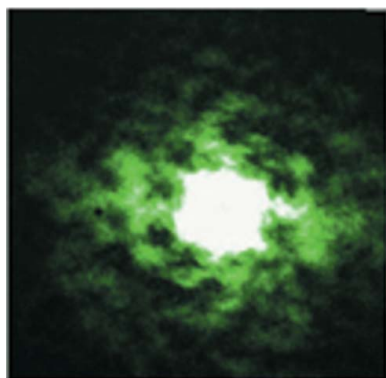
**Keywords:** STXM; spectronanoscropy; spectromicroscopy; soft X-ray fluorescence.

A scanning transmission X-ray microscope is operational at the 10A beamline at the Pohang Light Source. The 10A beamline provides soft X-rays in the photon energy range 100–2000 eV using an elliptically polarized undulator. The practically usable photon energy range of the scanning transmission X-ray microscopy (STXM) setup is from  $\sim 150$  to  $\sim 1600$  eV. With a zone plate of 25 nm outermost zone width, the diffraction-limited space resolution,  $\sim 30$  nm, is achieved in the photon energy range up to  $\sim 850$  eV. In transmission mode for thin samples, STXM provides the element, chemical state and magnetic moment specific distributions, based on absorption spectroscopy. A soft X-ray fluorescence measurement setup has been implemented in order to provide the elemental distribution of thicker samples as well as chemical state information with a space resolution of  $\sim 50$  nm. A ptychography setup has been implemented in order to improve the space resolution down to 10 nm. Hardware setups and application activities of the STXM are presented.

## 1. Introduction

Synchrotron radiation based X-ray absorption spectroscopy (XAS) measures absorbance changes as a function of incident X-ray energy and has become a very important probe for understanding physical and chemical properties of sample systems. XAS probes the energy position of orbitals and their unoccupied density of states, and as a result allows us to probe the kind of element, oxidation state, valence, atomic structure and bonding configuration in a sample (Stohr, 1992; Chen, 1997; de Groot, 1994). As nanometre- and micrometre-size devices and materials have emerged by the development of micro- and nanotechnology and as there is a huge amount of heterogeneous structures existing in our real world, there is a need for space-resolved spectroscopy (or spectromicroscopy, spectronanoscropy, microspectroscopy or nanospectroscopy), and the related technology has been developed (Attwood & Sakdinawat, 2016; Kirz *et al.*, 1995).

In the early 1990s, scanning transmission X-ray microscopy (STXM) was realized based on XAS in transmission mode, benefitting from the advent of Fresnel zone plate fabrication technology, the fast stage-scanning technique and fast photon detection technology (Kirz *et al.*, 1995). The space resolution of STXMs in those days was  $\sim 50$  nm and they were actively applied for providing space-resolved spectromicroscopic information on organic and chemically heterogeneous thin materials, magnetic thin films, and so on, by providing images obtained at chemically specific photon energies (Kirz *et al.*, 1995; Ade *et al.*, 1992; Warwick *et al.*, 1998). After the devel-



opment and implementation of laser interferometric encoding technology (Kilcoyne *et al.*, 2003), STXM functionality has improved greatly, especially with regard to accurate sample positioning and maintaining the focus position while changing the incident X-ray energy, and reliable, more user-friendly and practically competitive STXM setups have been developed worldwide (Kilcoyne *et al.*, 2003; Hitchcock *et al.*, 2008; Raabe *et al.*, 2008). Nowadays, the space resolution of STXM is  $\sim 30$  nm and this diffraction-limited focused spot size depends on the type of Fresnel zone plate (ZP). The space resolution can be improved down to 5–10 nm with the recently developed ptychography technique (Shapiro *et al.*, 2014; Menzel *et al.*, 2013).

At the Pohang Light Source (PLS), the 10A beamline was designed and built for STXM; the setup has been installed in the beamline and is now operational. Besides the nominal functionality of STXM (here, nominal functionality of STXM refers to STXM in transmission mode utilizing a focusing X-ray lens to obtain images and spectra) (Kirz *et al.*, 1995; Ade *et al.*, 1992; Warwick *et al.*, 1998; Kilcoyne *et al.*, 2003; Hitchcock *et al.*, 2008; Raabe *et al.*, 2008), a soft X-ray fluorescence measurement setup (Gianoncelli *et al.*, 2009; Kaulich *et al.*, 2009) has been implemented in order to provide elemental and chemical state information from samples thicker than those used for nominal STXM application in transmission mode, and a ptychography setup (Shapiro *et al.*, 2014; Menzel

*et al.*, 2013; Maiden *et al.*, 2013; Deng *et al.*, 2015) has been installed in order to achieve a space resolution down to 10 nm. Details of the nominal and the added functionalities of STXM at the PLS 10A beamline are described.

## 2. Beamline

The 10A beamline for STXM is an entrance-slit-less beamline having a modified SX-700-type plane-grating monochromator (Warwick *et al.*, 2004). A schematic of the beamline is shown in Fig. 1. In the beamline, soft X-rays are generated from an elliptically polarized undulator (EPU). The magnet array period and length of the undulator are 72 mm and 2.5 m, respectively. The X-rays are generated inside the undulator and are designed to be focused onto a fixed-exit slit (Exit Slit) by using a mirror (Mirror #2) in the vertical and horizontal directions. Another mirror (Mirror #1) turns diverging X-rays into non-diverging X-rays in the vertical direction and parallel to the ground floor. In between Mirror #1 and Mirror #2, a pre-mirror and two gratings are positioned. The gratings are switchable laterally perpendicular to the direction of the X-rays as shown in the figure. The pre-mirror, which is planar in shape, changes the incident angle of the X-rays towards the plane grating. The X-rays are then diffracted from the grating, and the diffracted X-rays with the desired photon energy propagate parallel to the ground floor, and are focused by

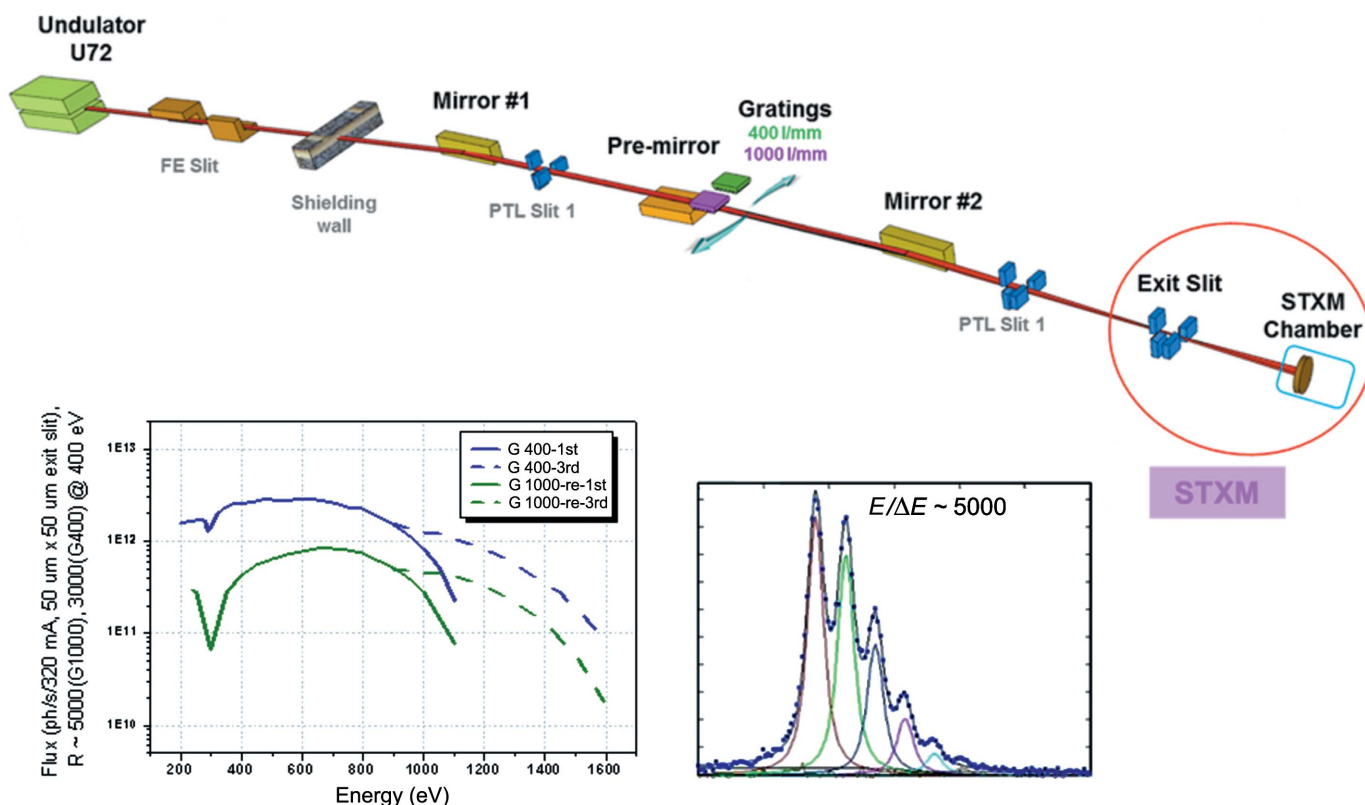


Figure 1

(Top) Schematic of an EPU beamline (10A) for STXM at the Pohang Light Source. Front-end (FE) and photon transfer line (PTL) slits are used to allow only the useful portion of X-rays to pass through. (Bottom left) Measured photon flux as a function of photon energy with 400 and 1000 lines  $\text{mm}^{-1}$  gratings. First-order and third-order harmonics are plotted. (Bottom right) N K-edge absorption spectrum obtained from molecular nitrogen: the spectral features of vibrational modes indicate that the spectral resolving power ( $E/\Delta E$ ) of the beamline is  $\sim 5000$ . The deconvoluted spectral lines are shown.

**Table 1**  
Parameters of the beamline optical components.

Item	Shape	Material	Coating	Incidence angle	Clear aperture	Other
Mirror #1	Cylindrical	Glidcop	60 nm Pt	2.5°	200 × 50 mm	
Pre-mirror	Planar	Silicon; internal cooling	60 nm Pt		430 × 76 mm	
Grating 1	Planar, 1000 lines mm <sup>-1</sup>	Silicon; side cooling	50 nm Au with Cr layer		150 × 33 mm	6 nm groove depth, 40% duty ratio
Grating 2	Planar, 400 lines mm <sup>-1</sup>	Silicon; side cooling	50 nm Au with Cr layer		150 × 33 mm	14 nm groove depth, 30% duty ratio
Mirror #2	Toroidal	Silicon	60 nm Pt	2.5°	200 × 50 mm	

Mirror #2 to the exit slit. Two gratings, 400 and 1000 lines mm<sup>-1</sup> gratings, are used. The exit slit behaves as a virtual source for STXM. The advantage of the modified SX-700-type monochromator is that the virtual source position is fixed independently of the X-ray photon energy. The distance from the exit slit to the Si<sub>3</sub>N<sub>4</sub> window, entry to the scanning transmission X-ray microscope, is 2.5 m. This Si<sub>3</sub>N<sub>4</sub> window is placed a few millimetres ahead of a focusing ZP. At an electron beam energy of 3 GeV in the storage ring, 340 mA, the photon flux measured after the 50 × 50 μm exit slit is 10<sup>11</sup>–10<sup>12</sup> photons s<sup>-1</sup> with the 400 lines mm<sup>-1</sup> grating and 10<sup>10</sup>–10<sup>11</sup> photons s<sup>-1</sup> with the 1000 lines mm<sup>-1</sup> grating. With this exit-slit width, the expected spectral resolving power,  $E/\Delta E$ , of the beamline is ~5000 at 400 eV. The measured spectrum from the vibration mode of molecular nitrogen, N<sub>2</sub>, is shown in the bottom right of Fig. 1, and the deconvoluted spectral feature results in a spectral resolving power of 5000. Besides the main optical components, the front-end slit and photon transfer line slits in the figure are employed in order to block stray or unwanted X-rays. After final alignment of the beamline, small changes of the source position (due to electron beam orbit changes inside a storage ring) are effectively compensated by adjusting Mirror #1. Parameters of the main optical components of the beamline are listed in Table 1.

### 3. STXM

The scanning transmission X-ray microscope at the 10A beamline is schematically the same as those of the Advanced Light Source (ALS) and Canadian Light Source (Kilcoyne *et al.*, 2003; Hitchcock *et al.*, 2008). The hardware was created by Bruker Ltd and the STXM control software was provided by Bruker Ltd: the software was originally written by Tolek Tyliczszak (ALS) and Peter Hitchcock (McMaster University) for the ALS STXM setup. Fig. 2 shows an assembly drawing of the main components (left) and a close-up view (right) showing a ZP, an order-sorting aperture (OSA), a sample holder and the front part of a photomultiplier tube (PMT) detector. The whole assembly is placed inside a vacuum STXM chamber. The main components are vacuum compatible and the base pressure of the STXM chamber is 1 × 10<sup>-5</sup> mbar (10<sup>-7</sup> mbar when baked out). In the figure, a rotatable sample mount is shown. In most experiments, a non-rotatable and kinematic mounting sample holder is used. After sample loading, in most experiments the STXM chamber is pumped down to ~10<sup>-1</sup> mbar and then filled with 20–100 mbar of He gas. One advantage of filling the STXM chamber with 20–100 mbar of He is an efficient heat dissipation from heat-generating components, such as stepping

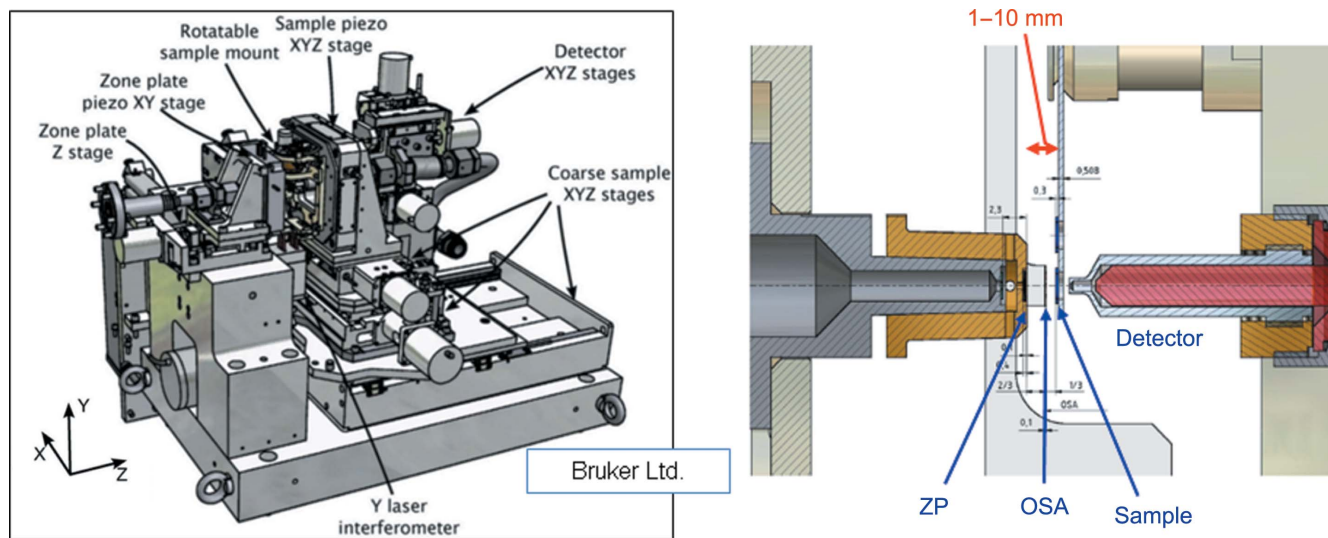


**Figure 2**  
(Left) Assembly drawing of the main components inside a STXM chamber. (Right) Schematic showing the main optical components: zone plate (ZP), order-sorting aperture (OSA), sample and front part of the detector.

motors and scanning stages. The focal length of the ZP is a linear function of the photon energy, and the ZP position needs to be adjusted towards or away from the sample along the  $z$  direction when one changes the photon energy. When the ZP stage moves along the  $z$  direction, an irregular position change occurs along the  $x$  and  $y$  directions, and this change needs to be compensated in order to keep the focal position in the same position in the sample. For this purpose, accurate position change measurement is achieved by using the laser interferometer-based position change measuring technique with two sets of mirrors which are attached to the ZP and the sample stages. This relatively unpredictable position change between the ZP and the sample along the  $x$  and  $y$  directions during the ZP  $z$ -directional movement, thus encoded by the laser interferometric technique, is compensated by the feedback system (Kilcoyne *et al.*, 2003). When the reflecting mirror surfaces have slope errors or are not perfectly parallel, effective drift of the focal point occurs in the  $x$ - $y$  plane when changing the photon energy; the amount of drift is of the order of  $\sim 1 \mu\text{m}$  for several tens to hundreds of eV photon energy change (equivalent to hundreds of micrometres to a few millimetres ZP focal length change). When one obtains stack images (series of images for different photon energies), this gradual drift can be effectively compensated by using image processing software (stack image processor *aXis2000* software package; <http://unicorn.mcmaster.ca/aXis2000.html>).

The X-rays diverge from the virtual source, the size of which is defined by the exit-slit opening, and pass through a silicon nitride ( $\text{Si}_3\text{N}_4$ ) window before entering the STXM chamber. The thickness of the  $\text{Si}_3\text{N}_4$  window is 100 nm and the window size is  $0.5 \times 0.5 \text{ mm}$ . Upstream of the  $\text{Si}_3\text{N}_4$  window is evacuated to ultrahigh vacuum (UHV). A ZP holder is placed downstream of the  $\text{Si}_3\text{N}_4$  window holder, as shown in Fig. 2. Both the  $\text{Si}_3\text{N}_4$  window holder and the ZP holder move together along the  $z$  direction *via* a stage (zone plate Z stage in the figure). As an OSA a pinhole is placed at an optimally chosen  $z$  position and this position becomes a reference for calculating the ZP and sample  $z$  positions. At a fixed photon energy, the ZP stage finds its optimized position by scanning the OSA aperture with a predetermined OSA set value (about 1/3 focal length from the focus). Then, the sample position is optimized for best focus by scanning the sample. The X-ray intensity passing through the sample is monitored by a detector. In typical transmission mode, counting mode is applied. The counting system comprises phosphor (P43, in most cases), an optical guide (Lucite) and a PMT (Hamamatsu Photonics, model R647P, head-on type, bialkali photocathode, spectral response on 300–650 nm). Phosphor is painted on the front surface of the optical guide and converts X-rays into visible light. The optical guide and the PMT head are sandwiched with

index coupling grease for an efficient transfer of visible light. The PMT's maximum count rate is  $\sim 10^7 \text{ Hz}$  and in normal operation we adjust the exit-slit width (normally  $\sim 10 \times 10 \mu\text{m}$ ) so that a count rate of  $10^5$ – $10^6$  is obtained. This count rate is achieved for the photon energy range up to  $\sim 1500 \text{ eV}$ .

In nominal transmission mode operation, in most cases, a ZP with an outermost zone width ( $\Delta r_n$ ) of 25 nm is used. The ZP diameter is 250  $\mu\text{m}$ , the central stop diameter is 120  $\mu\text{m}$ , and the thicknesses of the Au patterns and the central stop are 100 nm and 500 nm, respectively. The ZP is placed 2.5 m downstream from the exit slit. The focal length for this ZP at  $\sim 500 \text{ eV}$  is  $\sim 4 \text{ mm}$ . The exit slit width is  $\sim 10 \mu\text{m}$  at  $\sim 500 \text{ eV}$  and thus the diffraction-limited space resolution,  $1.22\Delta r_n \simeq 30 \text{ nm}$ , is obtainable when considering the ZP specification and demagnification of the optics geometry. When sample substructure is well defined, as shown in Fig. 3 (left), the STXM discriminates  $< 20 \text{ nm}$  structures. For this image acquisition, the photon energy was 570 eV and the field of view was  $1 \times 1 \mu\text{m}$ , with  $250 \times 250$  pixels with 10 ms dwell time per pixel. Usually, a 0.5–1 ms dwell time is used per pixel in obtaining the images. The images are scanned by either stepping motor driven stages or piezo actuator driven stages. The maximum field of view is  $10 \times 8 \text{ mm}$  with the stepping motor driven stages, and that with the piezo actuator driven stages is  $150 \times 150 \mu\text{m}$  in flying scan mode. The travel range of the ZP stage (stepping motor driven) along the  $z$  direction for focal length adjustment is  $\sim 8 \text{ mm}$ . In acquiring images, point-by-point acquisition mode as well as flying scan acquisition mode are available. In practical application, flying scan mode is preferred because it is much faster. Other types of ZPs are also used: a ZP with an outermost zone width of 40 nm (with 100  $\mu\text{m}$  diameter and 500 nm-thick central stop) and a ZP with an outermost zone width of 60 nm (with 100  $\mu\text{m}$  diameter and 1  $\mu\text{m}$ -thick central stop) are used for soft X-ray fluorescence detection and for ptychography.

The ZP focal length changes as the photon energy changes and, thus, when obtaining stack images or a spectrum, the ZP should be repositioned along the X-ray propagation ( $z$  direction) as the photon energy changes, while the OSA and

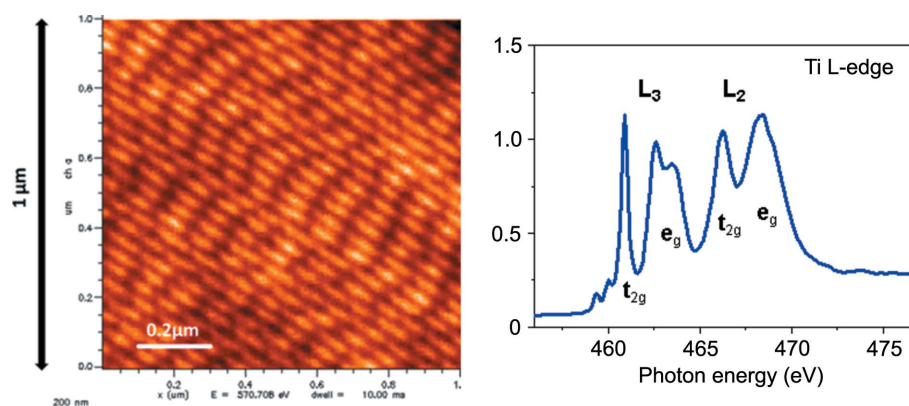


**Figure 3** (Left) STXM image of a test pattern. The field of view is  $1 \times 1 \mu\text{m}$ , with  $250 \times 250$  pixels. The photon energy was 570 eV. (Right) Spectrum obtained at the Ti  $L$ -edge from  $\text{TiO}_x$  nanometre-/micrometre-size particles, indicating that Ti is in anatase structure.

sample  $z$  remain at fixed positions. At a specific photon energy, one measures the photon intensity from a focused spot, or one records a line scan, or an image scan. By recording these data for different photon energies, one can obtain spectral information from the spot, or the spectral distribution along the line or within the image. As described above, as the ZP stage changes its position along the  $z$  direction, a focal point drift occurs in the  $x$  and  $y$  directions, mainly because of the imperfection of the surface figure and parallelism between the mirror surfaces attached in the ZP and sample moving stages. The drift is about  $1\ \mu\text{m}$ . If the region of interest or the domain size is smaller than  $1\ \mu\text{m}$ , then it is practically better to record an image stack and realign the stack images by using *aXis2000* software. From the realigned stack images, one can obtain spectral information from a spot or from a region of interest. The data on the right-hand side of Fig. 3 are from a Ti  $L$ -edge spectrum obtained from stack images of  $\text{TiO}_x$  particles dispersed onto a  $\text{Si}_3\text{N}_4$  window membrane. The Ti  $L$ -edge spectral features, the separation and shape of  $L_2$  and  $L_3$  and  $L_{2g}$  and  $e_g$  orbitals, clearly indicates that Ti particles are in anatase structure (Sharma *et al.*, 2015). The obtained images and spectra are routinely analysed using *aXis2000* software distributed by the spectromicroscopy community. STXM in transmission mode with  $\sim 30\ \text{nm}$  spatial resolution has been actively applied for nanometre- and micrometre-size functional materials, such as energy materials, battery materials, magnetic thin films (Handoko *et al.*, 2015), nano-bio materials (Nho *et al.*, 2014; Kim *et al.*, 2016), reactive oxygen generating cells (Yu *et al.*, 2018), and so on.

## 4. STXM with fluorescence measurement

An X-ray-induced fluorescence measurement gives the distribution of all the elements whose emission energy is lower than the incident X-ray energy and allows us to investigate thicker samples by probing the fluorescent layer which is several hundreds of nanometres below the sample surface. The fluorescence yield by soft X-rays is low, but the sensitivity of fluorescence detection is high ( $10^4$ – $10^5$ ) compared with that of STXM in transmission mode ( $\sim 10^2$ ) (Gianoncelli *et al.*, 2009; Kaulich *et al.*, 2009). A soft X-ray fluorescence detector was installed on the front side of the sample as shown in Fig. 4. An X-123SDD Amptek (<http://amptek.com/>) silicon drift detector, indicated as the MCA detector in the figure, with 25 mm active area and with a C2-type filter was installed for X-ray detection. The C2 filter passes lower photons down to boron (19.7%) and carbon (43.9%) fluorescence. The detector sensor head is Peltier cooled to 223 K. The energy resolution of the CCD is  $\sim 100\ \text{eV}$  at  $\sim 1000\ \text{eV}$  incident photon energy, which allows us to discriminate the elemental distribution of O, Mn, Co and Ni, as shown in Fig. 5 (bottom left). For an efficient collection of fluorescence, the sample holder was slightly bent towards the detector to  $\sim 20^\circ$  from the normal (unbent) sample plane, as shown in the figure.

In Fig. 5, one example of a STXM investigation measured by transmission and fluorescence modes for a  $\sim 3\ \mu\text{m}$ -size secondary-ion battery material is provided. The sample

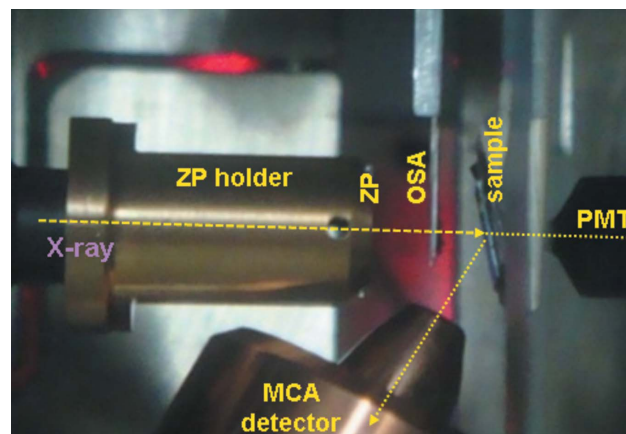


**Figure 4**  
Photograph near the sample showing the main optical components for the fluorescence measurement setup.

contains Ni, Co, Mn and O elements. The left-hand transmission image was obtained at 854 eV photon energy, just above the Ni  $L$ -edge, and it shows almost saturated absorption for all of the sample area, indicating that the sample is too thick for transmission mode measurement. The bottom-left data show fluorescence spectra obtained at a photon energy below and above the Ni  $L$ -edge absorption. The fluorescence spectrum obtained below the Ni absorption edge (red data obtained at 848 eV) shows a low Ni contribution, while Co, Mn and O contributions are detected. On the other hand, when the X-ray photon energy is at the Ni absorption edge, 854 eV, the Ni contribution becomes strong. The upper Ni, Mn and O fluorescence images shown in the figure were obtained at 854 eV incident photon energy. The dwell time per pixel was 200 ms. The field of view of the images was  $5.5 \times 5.5\ \mu\text{m}$  with  $200 \times 200$  pixels. The images show topological information because the detector is monitoring the sample at  $\sim 60^\circ$  from the surface normal. The fluorescence spectra in the figure (bottom left) were obtained from the sample. It is noticeable that the fluorescence yield just below and at the Ni  $L$ -edge (848 eV and 854 eV) also changes and near-edge X-ray absorption fine structure (NEXAFS) spectral information can be obtained by utilizing this fact. The data in the bottom right show an example of Mn  $L$ -edge NEXAFS spectra thus obtained from the sample by measuring the total fluorescence yield as a function of incident photon energy. In the data, Mn fluorescence yield was measured and the valence of the Mn obtained from the spectrum is 4+ (Lin *et al.*, 2014). Another spectrum was repeatedly measured in the earlier part of the photon energy, 635–650 eV, for the  $L_3$ -edge (blue data in the figure) and the result is the same. For the fluorescence measurement setup, a ZP with 40 nm outermost zone width was used and  $\sim 50\ \text{nm}$  spatial resolution is achieved in the fluorescence mode.

## 5. STXM for ptychography

Ptychography has developed rapidly over the past few years especially in the STXM setup, in order to achieve a better

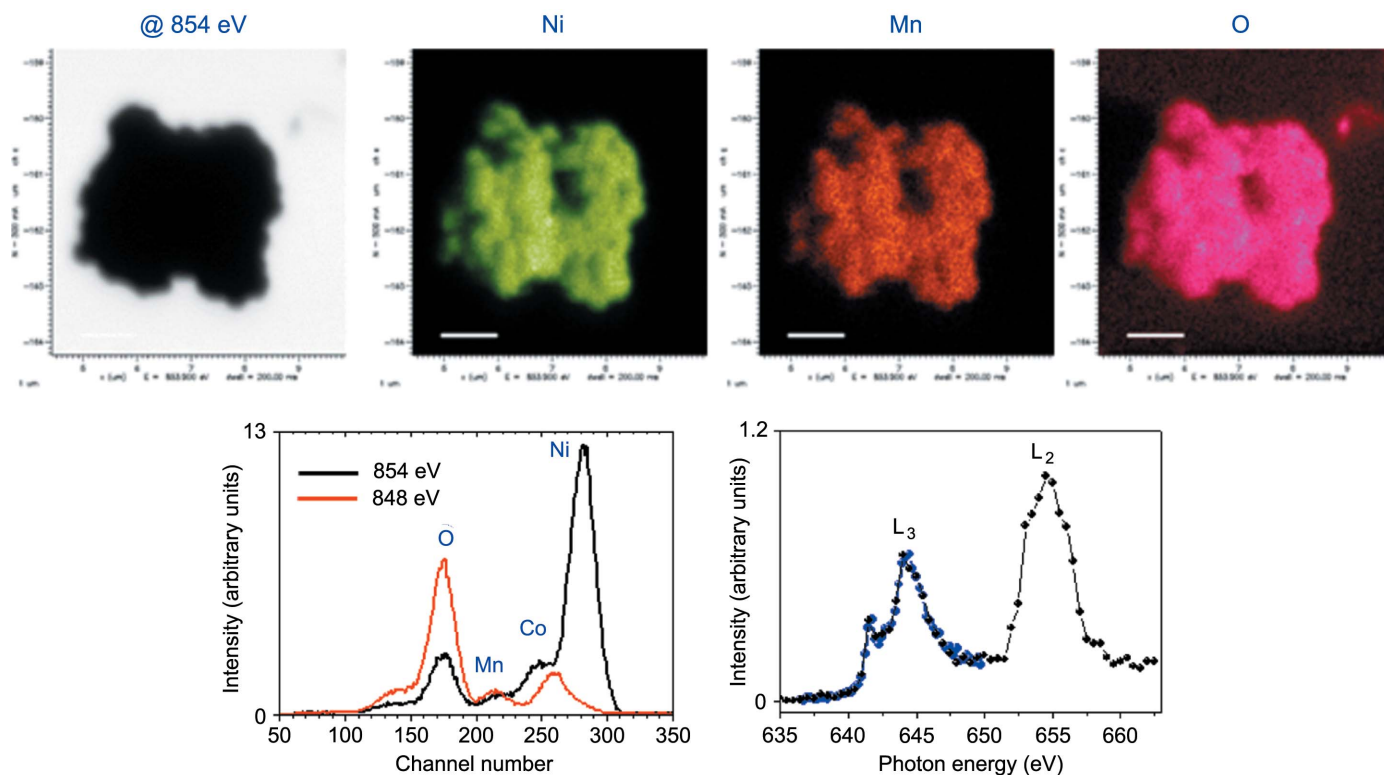


**Figure 5**

(Top left) An absorption contrast image obtained from a secondary-ion battery material, containing O, Mn, Co and Ni elements. The photon energy is 854 eV at the Ni  $L$ -edge. (Top: Ni, Mn, O images) Ni, Mn and O fluorescence images obtained from the sample with 854 eV photons, showing the distribution of Ni, Mn and O elements. Scale bar: 1  $\mu\text{m}$ . (Bottom left) Fluorescence spectra obtained at a photon energy below and at the Ni  $L$ -edge, 854 and 848 eV, respectively. O, Co, Mn elements are observed with 848 eV photons. With 854 eV photons, strong Ni fluorescence is observed. (Bottom right) Mn  $L$ -edge spectra obtained by measuring the Mn fluorescence yield as a function of incident photon energy. Repeated measurement at the  $L_3$ -edge region, 835–850 eV photon energy, is plotted (blue data).

spatial resolution than that obtained currently using focusing optics (Shapiro *et al.*, 2014; Menzel *et al.*, 2013; Gianoncelli *et al.*, 2009; Kaulich *et al.*, 2009; Maiden *et al.*, 2013). A ptychography setup has been installed as shown in Fig. 6, where a back-illumination-type CCD (Andor DX434-BN) was mounted replacing the PMT setup. In the figure, a cap attached to the CCD is shown. The CCD surface is  $\sim 80$  mm away from the sample plane. The pixel size of the CCD is  $13 \times 13 \mu\text{m}$  with  $1024 \times 1024$  active pixels. The 16 bit frame readout rate at 1 MHz is  $0.9 \text{ s}^{-1}$ . In the experiment, the chamber was evacuated and filled with a few tens of mbar of He gas. The CCD was cooled to 243 K. As an illuminating lens, a ZP with 60 nm outermost zone width is used, with a 1  $\mu\text{m}$ -thick central stop for an efficient block of zeroth-order X-rays. In the figure, on the right-hand side, several diffraction patterns obtained from nanometre- and micrometre-size  $\text{FeO}_x$  particles at the Fe  $L$ -absorption edge, 710 eV, are shown. The patterns are shown on a linear scale, indicating an efficient scattering coefficient for the measurement. The patterns were obtained in the Fresnel diffraction mode, in which the sample is positioned in the plane of the ZP focus. The acquisition time for each diffraction pattern was 200 ms. Based on the geometry we expect  $<10$  nm space resolution for the diffraction images. Currently, a reconstruction algorithm is under development.

## 6. Summary and discussion

STXM is operational at the 10A beamline at the PLS. The nominal STXM mode based on transmission X-ray measurement by using a PMT provides diffraction-limited space resolution ( $\sim 30$  nm with a ZP with 25 nm outermost zone width) with  $\sim 5000$  spectral resolving power. The helicity of X-rays from the EPU enables us to investigate magnetic materials in thin film geometry (Handoko *et al.*, 2015). A soft X-ray fluorescence detection mode has been implemented to measure fluorescence from a thick sample at a space resolution of  $\sim 50$  nm. Lastly, a ptychography mode, with a ZP with 60 nm outermost zone width, has been implemented for a better space resolution smaller than 10 nm.

## Acknowledgements

We would like to acknowledge Se Hee Lee, Si Woo Lee, Dr H. W. Noh, Professor T. H. Yoon and especially Dr Tolek Tyliszczak.

## Funding information

The authors would like to acknowledge the support of the Basic Science Research Program (NRF-2015R1A5A1009962)

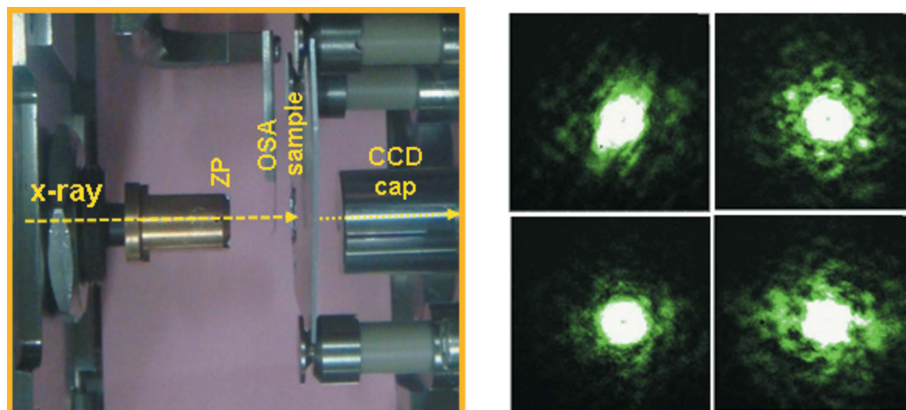


**Figure 6**  
 (Left) Photograph near the sample for the ptychography measurement setup. A CCD cap is shown. The CCD surface is placed ~80 mm away from the sample plane. (Right) Diffraction patterns obtained with 710 eV photon energy from FeO<sub>x</sub> nanometre- and micrometre-size particles. The images are plotted on a linear scale.

through the National Research Foundation of Korea funded by the Korea government Ministry of Science, ICT and Future Planning (MSIP).

**References**

Ade, H., Zhang, X., Cameron, S., Costello, C., Kirz, J. & Williams, S. (1992). *Science*, **258**, 972–975.  
 Attwood, D. & Sakdinawat, A. (2016). *X-rays and Extreme Ultraviolet Radiation: Principles and Applications*. Cambridge University Press.  
 Chen, J. G. (1997). *Surf. Sci. Rep.* **30**, 1–152.  
 Deng, J., Vine, D. J., Chen, S., Nashed, Y. S. G., Jin, Q., Phillips, N. W., Peterka, T., Ross, R., Vogt, S. & Jacobsen, C. (2015). *Proc. Natl Acad. Sci. USA*, **112**, 2314–2319.  
 Gianoncelli, A., Kaulich, B., Alberti, R., Klatka, T., Longoni, A., de Marco, A., Marcello, A. & Kiskinova, M. (2009). *Nucl. Instrum. Methods Phys. Res. A*, **608**, 195–198.  
 Groot, F. M. F. de (1994). *J. Electron Spectrosc. Relat. Phenom.* **67**, 529–622.  
 Handoko, D., Quach, D.-T., Lee, S.-H., Shim, J., Kim, D.-H., Lee, K.-M., Jeong, J.-R., Kim, N. & Shin, H.-J. (2015). *J. Kor. Phys. Soc.* **66**, 1732–1735.

Hitchcock, A. P., Dynes, J. J., Johansson, G., Wang, J. & Botton, G. (2008). *Micron*, **39**, 741–748.  
 Kaulich, B., Gianoncelli, A., Beran, A., Eichert, D., Kreft, I., Pongrac, P., Regvar, M., Vogel-Mikus, K. & Kiskinova, M. (2009). *J. R. Soc. Interface*, **6**(Suppl. 5), S641–S647.  
 Kilcoyne, A. L. D., Tyliczszak, T., Steele, W. F., Fakra, S., Hitchcock, P., Franck, K., Anderson, E., Harteneck, B., Rightor, E. G., Mitchell, G. E., Hitchcock, A. P., Yang, L., Warwick, T. & Ade, H. (2003). *J. Synchrotron Rad.* **10**, 125–136.  
 Kim, Y. W., Yang, S., Jeon, E. H., Baik, J. Y., Kim, N., Kim, H. S. & Lee, H. (2016). *Nanoscale Res. Lett.* **11**, 41.  
 Kirz, J., Jacobsen, C. & Howells, M. (1995). *Q. Rev. Biophys.* **28**, 33–130.  
 Lin, F., Markus, I. M., Nordlund, D., Weng, T.-C., Asta, M. D., Xin, H. L. & Doeff, M. M. (2014). *Nat. Commun.* **5**, 3529.  
 Maiden, A. M., Morrison, G. R., Kaulich, B., Gianoncelli, A. & Rodenburg, J. M. (2013). *Nat. Commun.* **4**, 1669.  
 Menzel, A., Diaz, A. & Guizar-Sicairos, M. (2013). *Synchrotron Radiat. News*, **26**, 26–31.  
 Nho, H. W., Kim, J. Y., Wang, J., Shin, H.-J., Choi, S.-Y. & Yoon, T. H. (2014). *J. Synchrotron Rad.* **21**, 170–176.  
 Raabe, J., Tzvetkov, G., Flechsig, U., Böge, M., Jaggi, A., Sarafimov, B., Vernooij, M. G. C., Huthwelker, T., Ade, H., Kilcoyne, D., Tyliczszak, T., Fink, R. H. & Quitmann, C. (2008). *Rev. Sci. Instrum.* **79**, 113704.  
 Shapiro, D. A., Yu, Y.-S., Tyliczszak, T., Cabana, J., Celestre, R., Chao, W., Kaznatcheev, K., Kilcoyne, A. L. D., Maia, F., Marchesini, S., Meng, Y. S., Warwick, T., Yang, L. L. & Padmore, H. (2014). *Nat. Photon.* **8**, 765–769.  
 Sharma, A., Varshney, M., Park, J., Ha, T.-K., Chae, K.-H. & Shin, H.-J. (2015). *RSC Adv.* **5**, 21762–21771.  
 Stohr, J. (1992). *NEXAFS Spectroscopy*. Berlin, Heidelberg: Springer-Verlag.  
 Warwick, T. et al. (1998). *Rev. Sci. Instrum.* **69**, 2964–2973.  
 Warwick, T., Andresen, N., Comins, J., Kaznatcheyev, K., Kortright, J. B., McKean, J. P., Padmore, H. A., Shuh, D. K., Stevens, T. & Tyliczszak, T. (2004). *AIP Conf. Proc.* **705**, 458–461.  
 Yu, S. U., Lee, H., Cho, W. J., Kim, C., Kang, M. C., Shin, H.-J., Kim, N., Hahn, S. K., & Kim, K. S. (2018). *Nanoscale.*, **10**, 150–157.